Assessing non-Oberbeck-Boussinesq effects of convection in cryogenic helium

Michal Macek [1], Georgy Zinchenko [2], Věra Musilová [1], Pavel Urban [1], and Jörg Schumacher [2,3]

[1] *The Czech Academy of Sciences, Institute of Scientific Instruments, CZ-61264 Brno, Czech Republic*

[2] *Institut für Thermo- und Fluiddynamik, Technische Universität Ilmenau, Postfach 100565, D-98684 Ilmenau, Germany*

[3] *Tandon School of Engineering, New York University, New York City, New York 11201, USA*

(Received 24 May 2023; accepted 24 August 2023; published 26 September 2023)

The present study investigates the non-Oberbeck-Boussinesq (NOB) effects which arise due to the temperature dependence of material properties in cryogenic helium experiments of turbulent Rayleigh-Bénard convection. Here we quantify these effects solely by the difference of the measured mean temperature at the center of the closed cell, T_c, from the arithmetic mean temperature obtained from the prescribed fixed and uniform temperatures at the top and bottom copper plates of the apparatus, $T_m = (T_{\rm bot} + T_{\rm top})/2$. To this end, the material properties such as specific heat at constant pressure, dynamic viscosity, thermal conductivity, the isobaric expansivity, and the mass density are expanded into power series with respect to temperature up to the quadratic order with coefficients obtained from the software package HEPAK. A subsequent nonlinear regression that uses deep convolutional networks delivers a dependence of the strength of non-Oberbeck-Boussinesq effects in the pressure-temperature parameter plane. Strength of the NOB effects is evaluated via the deviation of the mean temperature profile $\xi_{\rm NOB} \equiv T_m - T_c$ from the top-bottom-symmetric Oberbeck-Boussinesq case $\xi_{\rm NOB} = 0$. Training data for the regression task are obtained from 236 individual long-term laboratory measurements at different Rayleigh numbers which span eight orders of magnitude.

DOI: 10.1103/PhysRevFluids.8.094606

I. INTRODUCTION

Controlled laboratory experiments of turbulent Rayleigh-Bénard convection (RBC) are one pillar of turbulence research to obtain a deeper understanding of the physical transfer processes and their coupling to statistical properties and structures, both in the bulk and the boundary layers of buoyancy-driven flows [1–4]. The highest Rayleigh numbers Ra for fluid flows at Prandtl numbers $\mathrm{Pr} \simeq 1$ are obtained in two gases, either compressed sulfur hexafluoride, SF_6 [5,6], or cryogenic helium, ^{4}He, the latter of which is cooled down to a few Kelvin [7–14]. While the Rayleigh number Ra quantifies the thermal driving of convective turbulence, the Prandtl number Pr is the ratio of molecular momentum to temperature diffusion. Together with a third parameter, the aspect ratio of the exclusively used cylindrical closed vessels $\Gamma = D/H$ with cell diameter D and cell height H, these three dimensionless numbers determine the control parameters of the experiments and are subsequently used to quantify the response. of the apparatus in the form of power laws of the turbulent momentum and heat transfer. The latter are quantified by the dimensionless Reynolds and Nusselt numbers, Re and Nu [2,3]. The present study is focused to the experiments in cryogenic helium, ^{4}He.

The Rayleigh-Bénard convection model incorporates the Oberbeck-Boussinesq (OB) approximation [3,4] which considers the working fluid as incompressible. In addition, the mass density

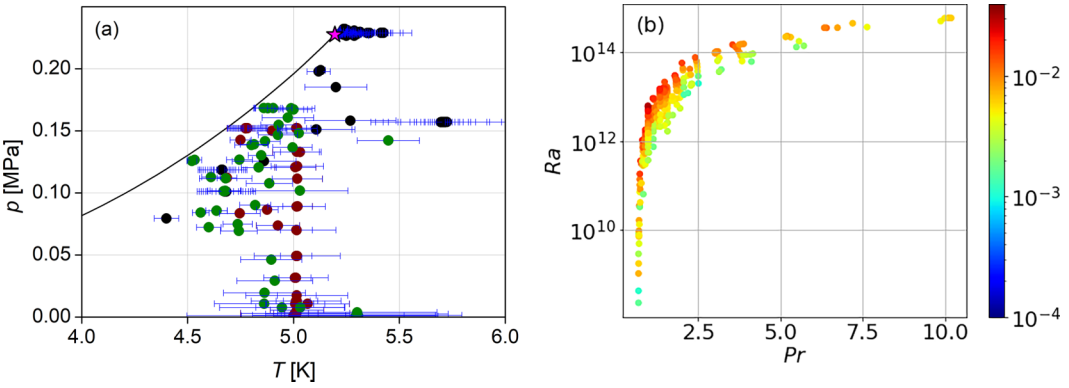

FIG. 1. Summary of the operating points (p_m, T_m) of the cryogenic Rayleigh-Bénard experiments. (a) The mean temperatures T_m and the temperature range $\Delta T = T_{\rm bot} - T_{\rm top}$ at a mean pressure p_m are provided in the p-T parameter plane. The "error bars" stemming from the (p_m, T_m) points denote the ranges of ΔT between the cold (blue) and hot (red) plate temperatures T_t, T_b, respectively. The solid line marks the saturated vapor curve (SVC) and the star symbol in the center of the figure indicates the critical point (CP) with $T_{\rm cri} = 5.195$ K, $p_{\rm cri} = 0.228$ MPa. The different colors of experimental (p_m, T_m) points correspond to new data (green), and data published in Refs. [15] (black) and [16] (brown). (b) Color-coded non-Boussinesq parameter $\xi_{\rm NOB}$ at the Ra, Pr control parameters for the experiments shown in panel (a), given in units of Kelvin.

field of the fluid, $\rho(\boldsymbol{x}, t)$ is taken as a linear function of the temperature field $T(\boldsymbol{x}, t)$ and given by

$$\rho(\boldsymbol{x}, t) = \rho_{\rm ref}\{1 - \alpha[T(\boldsymbol{x}, t) - T_{\rm ref}]\} \quad \text{with} \quad \alpha = -\frac{1}{\rho}\frac{\partial \rho}{\partial T}\bigg|_p, \tag{1}$$

with the isobaric thermal expansion coefficient or expansivity α. This dependence is incorporated in the volume forces and thus couples the temperature field to the momentum balance. Quantities $\rho_{\rm ref}$ and $T_{\rm ref}$ are reference magnitudes of density and temperature, respectively. One important consequence of the OB approximation is that statistical properties, such as mean profiles, in the lower and upper halves of the convection cell including the corresponding viscous and thermal boundary layers, are symmetric with respect to the midplane at $z = H/2$. Consequently,

$$T_c := \left\langle T\left(z = \frac{H}{2}\right)\right\rangle = \frac{T_{\rm bot} + T_{\rm top}}{2} =: T_m, \tag{2}$$

in laboratory experiments with the prescribed fixed and uniform temperatures at the top and bottom, $T_{\rm top}$ and $T_{\rm bot}$.

Cryogenic RBC experiments at the highest Rayleigh numbers have to be operated close to the critical point (CP) of He [8,11–13]. At this point, where the saturated vapor curve (SVC) representing the phase boundary between the gas and liquid state ends, the material properties of the working fluid such as specific heat at constant pressure, C_p, dynamic viscosity μ, or thermal conductivity λ fluctuate strongly. This is considered as one possible source of the deviations from the Boussinesq limit, which are experimentally probed by a violation of (2). In other words, non-Boussinesq (NOB) effects are detected as $T_c \neq T_m$. It is exactly this deviation which we want to explore in detail in the present work for cryogenic ^{4}He. Therefore, we define the non-Oberbeck-Boussinesq parameter,

$$\xi_{\rm NOB}(p_m, T_m, \chi_k) := T_m - T_c, \tag{3}$$

where χ_k are for now a short-hand notation for material properties which will be specified further below. Figure 1(a) summarizes the operating points within the p-T diagram for cryogenic experiments conducted in the apparatus of the group in Brno (Czech Republic) [17]. We indicate the mean

temperature as well as the range of the applied outer temperature difference $\Delta T = T_{\mathrm{bot}} - T_{\mathrm{top}} > 0$ at the mean pressure $p = p_m$. It is seen that a number of measurements are close to the phase boundary (solid black curve) and a few even in the vicinity of the critical point (magenta star). In Fig. 1(b), the measured values of ξ_{NOB} are plotted in the phase diagram of the two control parameters, Ra and Pr. It is important to note that Ra and Pr are control parameters characterizing OB convection, thus ideally $\xi_{\mathrm{NOB}} = 0$ independent of Ra and Pr. The experimentally observed values $\xi_{\mathrm{NOB}} \neq 0$ unambiguously indicate presence of NOB effects and must be captured introducing additional control parameters. We define and discuss a suitable set below.

In this work, we will systematically investigate the non-Boussinesq effects in cryogenic helium experiments at high Rayleigh numbers spanning a range of $10^7 \lesssim \mathrm{Ra} \lesssim 10^{15}$ performed in Brno. We quantify the deviation of the center temperature T_c from T_m in the p-T diagram by means of nonlinear regression applying deep neural networks, i.e., determine $\xi_{\mathrm{NOB}}(p_m, T_m)$. This regression proceeds in three different levels of refinement, partly based on a perturbative expansion of the temperature dependence of essential material parameters and state variables p, T as described in the next section. Furthermore, we aim to identify which of the variations of the material parameters are the most important ones for the magnitude of the NOB parameter. The complex material dependencies including discontinuities at the phase boundary and the singularities at the critical point are tabulated in the software package HEPAK written by V. Arp *et al.* [18] and retailed by Horizon Technologies Inc. [19]. They allow us to quantify the prefactors of the polynomial expansions of the material parameters and state variables at different orders. The starting point is the set of fully compressible equations of motion which was outlined by Gray and Giorgini [20]. Material parameter dependencies have been also systematically discussed for high-Rayleigh-number experiments in compressed SF_6 in Refs. [21–23].

We mention that other response parameters typically studied in RBC, such as the Nusselt number Nu and the Reynolds number Re, may in contrast to ξ_{NOB} deviate from predictions of OB models of RBC due to hydrodynamical effects. The latter can arise for example from the growing level of fluctuations inside the boundary layers as discussed in Refs. [2,3]. They are thus not related to NOB behavior. Also, we will show that compressibility effects, which add a further component to NOB behavior, can be excluded for the present cell height and pressures. In this work, the NOB effects will be solely quantified by ξ_{NOB}.

Our paper is organized as follows. Section II introduces the fully compressible equations of motion and discusses the resulting polynomial expansions for the material properties. In Sec. III, we explore the basic state and transport properties of ^{4}He as a function of pressure p and temperature T in connection with the (p_m, T_m) operating points of all realized RBC experiments within the respective ΔT region. Here we also discuss the second mechanism to NOB convection, the compressibility effects which are shown to be negligible in the present setup. In Sec. IV, we briefly overview the essential features of the experimental set-up for cryogenic RBC. Section V discusses the nonlinear regression results. In the last section, we give the conclusions and outlook. Technical details of the deep neural networks and an error analysis of the machine learning procedures are discussed in Appendices A and B.

II. PERTURBATIVE EXPANSION OF THE EQUATIONS OF MOTION

Convective motions in a fluid layer are described by the set of three balance equations involving the continuity equation for the mass balance, the Navier-Stokes equations for the momentum balance, and the energy balance equation. Following here the textbook by Batchelor [24] and the seminal work by Gray and Giorgini [20], they are given by

$$\frac{D\rho}{Dt} = -\rho \frac{\partial u_j}{\partial x_j}, \tag{4}$$

$$\rho \frac{Du_i}{Dt} = -\frac{\partial p}{\partial x_i} - \rho g_i \alpha T + \frac{\partial}{\partial x_j}(\mu \Gamma_{ij}), \tag{5}$$

$$\rho C_p \frac{DT}{Dt} - \alpha T \frac{Dp}{Dt} = \frac{\partial}{\partial x_j}\left(\lambda \frac{\partial T}{\partial x_j}\right) + \mu\Phi, \tag{6}$$

where $D\bullet/Dt = \partial\bullet/\partial t + \boldsymbol{u}\cdot\nabla\bullet$ is the material derivative and

$$\Gamma_{ij} = \frac{\partial u_i}{\partial x_j} + \frac{\partial u_j}{\partial x_i} - \frac{2}{3}\frac{\partial u_k}{\partial x_k}\delta_{ij} \tag{7}$$

is the rate of strain tensor in the compressible case. Furthermore,

$$\Phi = \frac{1}{2}\Gamma_{ij}\left(\frac{\partial u_i}{\partial x_j} + \frac{\partial u_j}{\partial x_i}\right), \tag{8}$$

is the dissipation function and $g_i = (0, 0, -g)$ the vector that contains the acceleration due to gravity g in vertical direction. The bulk viscosity is set to zero.

A simplified form of the convection equations (4)–(6) is obtained in the form of the OB approximation, once the dynamical viscosity μ, the thermal conductivity λ, the isobaric thermal expansivity α, and the specific heat C_p at constant pressure are taken as constants. Furthermore, the mass density is taken to be constant $\rho = \rho_0$, such that the flow is basically incompressible, and heating due to pressure variations remains subdominant, which results in

$$\frac{\partial u_j}{\partial x_j} = 0, \tag{9}$$

$$\rho_0 \frac{Du_i}{Dt} = -\frac{\partial p}{\partial x_i} - \rho_0 g_i \alpha T + \mu \frac{\partial^2 u_i}{\partial x_j^2}, \tag{10}$$

$$\rho C_p \frac{DT}{Dt} = \lambda \frac{\partial^2 T}{\partial x_j^2}. \tag{11}$$

This implies that the speed of sound is much larger than the typical convection velocity, the free-fall velocity $U_f = \sqrt{g\alpha\Delta T H}$ for small $\alpha\Delta T$. In all expressions above we have used the Einstein summation convention.

Our objective is to evaluate the importance of individual terms of the compressible equations (4)–(6) beyond the OB limit systematically and analyze their effects on the mean temperature profiles in the thermal convection experiments in cryogenic helium. We will therefore assume that all material parameters are functions of the temperature only and that their pressure dependence is much less significant for the present experimental conditions. They can then be approximated by Taylor expansions with respect to T, which we will follow up to the quadratic expansion term. This results to the following expressions:

$$\rho = \rho_0(1 - \alpha_0\delta T + \beta_0\delta T^2), \tag{12}$$

$$\mu = \mu_0(1 + m_{10}\delta T + m_{20}\delta T^2), \tag{13}$$

$$C_p = C_{p0}(1 + c_{10}\delta T + c_{20}\delta T^2), \tag{14}$$

$$\lambda = \lambda_0(1 + l_{10}\delta T + l_{20}\delta T^2), \tag{15}$$

$$\alpha = \alpha_0(1 + a_{10}\delta T + a_{20}\delta T^2). \tag{16}$$

where $\delta T = T - T_m$. The first index in coefficients defines the term number in Taylor series decomposition, index 0 refers to the mean temperature T_m and the minus in (12) follows a convention usual in fluid dynamics. All constants in the expansions (12)–(16) are determined from quadratic interpolations of the respective material properties at three temperature values T_{top}, T_m, and T_{bot} at a given pressure value p using HEPAK [18].

TABLE I. List of all Taylor expansion parameters ε_i for $i = 1, \ldots, 10$.

Quantity	First-order expansion	Second-order expansion
Mass density, ρ	$\varepsilon_1 = \alpha_0 \Delta T$	$\varepsilon_2 = \beta_0 \Delta T^2$
Dynamic viscosity, μ	$\varepsilon_3 = m_{10} \Delta T$	$\varepsilon_4 = m_{20} \Delta T^2$
Specific heat, C_p	$\varepsilon_5 = c_{10} \Delta T$	$\varepsilon_6 = c_{20} \Delta T^2$
Thermal conductivity, λ	$\varepsilon_7 = l_{10} \Delta T$	$\varepsilon_8 = l_{20} \Delta T^2$
Isobaric expansion coefficient, α	$\varepsilon_9 = a_{10} \Delta T$	$\varepsilon_{10} = a_{20} \Delta T^2$

The substitution of Eqs. (12)–(16) into the compressible fluid equations (4)–(6) and the subsequent performance of a number of transformations leads to a set of a dimensionless convection equations which include the NOB effects up to second order with respect to temperature. They are given by

$$-\varepsilon_1 \frac{D\theta}{Dt} + 2\varepsilon_2 \theta \frac{D\theta}{Dt} = -(1 - \varepsilon_1 \theta + \varepsilon_2 \theta^2) \frac{\partial u_j}{\partial x_j}, \tag{17}$$

$$(1 - \varepsilon_1 \theta + \varepsilon_2 \theta^2) \frac{Du_i}{Dt} = -\frac{\partial (p - p_s)}{\partial x_i} + \left[(\theta - \theta_s) - \frac{\varepsilon_2}{\varepsilon_1} \left(\theta^2 - \theta_s^2 \right) \right] k_i + \frac{1}{\mathrm{Re}_f} (1 + \varepsilon_3 \theta + \varepsilon_4 \theta^2) \frac{\partial \Gamma_{ij}}{\partial x_j} + \frac{1}{\mathrm{Re}_f} (\varepsilon_3 + 2\varepsilon_4 \theta) \Gamma_{ij} \frac{\partial \theta}{\partial x_j}, \tag{18}$$

$$(1 - \varepsilon_1 \theta + \varepsilon_2 \theta^2)(1 + \varepsilon_5 \theta + \varepsilon_6 \theta^2) \frac{D\theta}{Dt} = \frac{\tilde{D}}{\mathrm{Re}_f} (1 + \varepsilon_3 \theta + \varepsilon_4 \theta^2) \Phi + \frac{1}{\mathrm{Re}_f \mathrm{Pr}} (1 + \varepsilon_7 \theta + \varepsilon_8 \theta^2) \frac{\partial^2 \theta}{\partial x_j^2} + \frac{1}{\mathrm{Re}_f \mathrm{Pr}} (\varepsilon_7 + 2\varepsilon_8 \theta) \left(\frac{\partial \theta}{\partial x_j} \right)^2 + \tilde{D} (1 + \varepsilon_9 \theta + \varepsilon_{10} \theta^2) \times \left[\varepsilon_1 \frac{D(p - p_s)}{Dt} - \left(1 - \varepsilon_1 \theta_s + \varepsilon_2 \theta_s^2 \right) u_3 \right] (\theta + \tilde{T}_m). \tag{19}$$

Here

$$\theta = \frac{\delta T}{\Delta T} = \frac{T - T_m}{T_{\mathrm{bot}} - T_{\mathrm{top}}} \quad \text{and} \quad \tilde{T}_m = \frac{T_m}{\Delta T} = \frac{T_m}{T_{\mathrm{bot}} - T_{\mathrm{top}}}, \tag{20}$$

and θ_s and p_s are temperature and pressure equilibrium (static heat conduction) profiles, respectively. Furthermore, we define in the energy balance a dimensionless parameter

$$\tilde{D} = \frac{g \alpha_0 H}{C_{p0}}, \tag{21}$$

which is denoted as the dissipation number [25]. This number relates the dry adiabatic lapse rate g/C_{p0} to the characteristic temperature drop $\alpha_0 H$. The velocity was made nondimensional by U_f. The Prandtl number reads $\mathrm{Pr} = \nu_0/\kappa_0$ with the temperature diffusivity $\kappa_0 = \lambda_0/(\rho_0 C_{p0})$, the free-fall Reynolds number $\mathrm{Re}_f = U_f H/\nu_0$, and the unit vector in the momentum balance points into the positive z direction, $k_i = (0, 0, 1)$. The free-fall Reynolds number follows to $\mathrm{Re}_f = \sqrt{\mathrm{Ra}/\mathrm{Pr}}$ where Ra is the Rayleigh number

$$\mathrm{Ra} = \frac{\alpha_0}{\nu_0 \kappa_0} g \Delta T H^3. \tag{22}$$

Finally, in Table I, we list all parameters ε_i which were used in Eqs. (17)–(19) for first- and second-order expansions. Setting all these expansion parameters ε_i and $\tilde{D}$ to zero recovers the OB equations (9)–(11) [2,3]. Expansion parameters with an odd-number index are for the linear

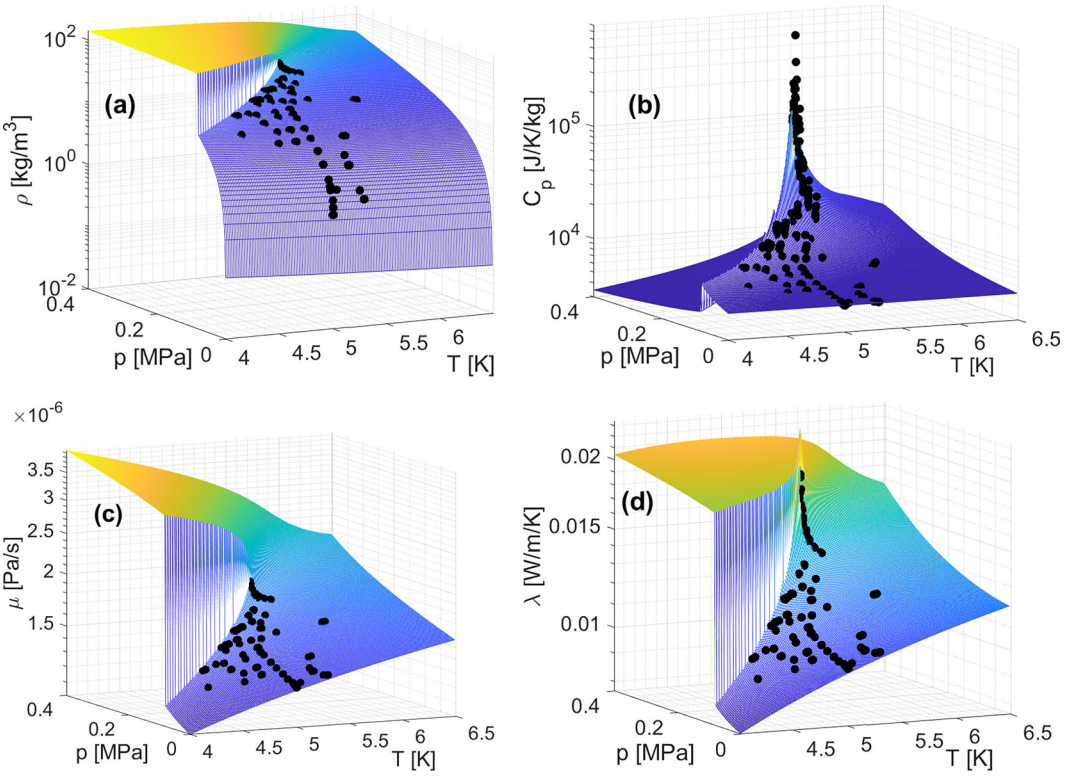

FIG. 2. Basic state quantities [(a) and (b)] and molecular transport properties [(c) and (d)] which characterize the complex material properties of cryogenic helium ^{4}He near its critical point (CP) of $p_{\mathrm{CP}} = 227$ kPa and $T_{\mathrm{CP}} = 5.2$ K as a function of pressure p and temperature T. (a) The density ρ which thus corresponds with the equation of state $\rho(T, p)$. (b) The specific heat C_p, (c) the dynamical viscosity μ, and (d) the thermal conductivity λ. The black bullets indicate the mean values p_m and T_m for all experiments shown in Fig. 1. The data are obtained from the HEPAK code [18].

expansion while those with an even index are for the quadratic order. Notice that $\tilde{D}$, similar to the OB control parameters Ra and Pr depends only on local values of the material properties at the reference temperature T_m, and—like the Prandtl number Pr—is independent of ΔT. In this sense it differs from ε_i, which are "nonlocal" and depend on the temperature derivatives at T_m as well as ΔT. The regression algorithms in Sec. V will proceed in incremental steps, i.e., consider linear expansions only at first and incorporate second-order subsequently.

III. STATE AND TRANSPORT PROPERTIES OF CRYOGENIC ^{4}He

Figure 2 shows the accurate values of the mass density ρ, the specific heat at constant pressure C_p, the dynamic viscosity μ, and the thermal conductivity λ with respect to the p-T plane in a region of gaseous helium phase including the regions near to the vapor liquid saturation curve and the critical point. These surfaces are obtained from the HEPAK code [18], which is based on high-order interpolation of all available and reliable measurements. The plots give us a first guidance in the selection of the appropriate the functional form of the state and transport properties in the equations beyond the OB approximation. All displayed quantities, ρ, C_p, λ, and μ develop a discontinuity at the phase boundary in the pressure-temperature plane which corresponds to a first-order gas-liquid phase transition. Furthermore, C_p and λ develop a divergence at the CP, which is given by $p_{\mathrm{CP}} = 227$ kPa and $T_{\mathrm{CP}} = 5.2$ K. The precursors of this divergence are visible here.

Panel (a) displays in fact the equation of state $\rho(T, p)$. In the vicinity of this point, most of the RBC experiments in cryogenic helium have been performed as indicated by the black dots in all panels of the figure. They indicate mean pressure and temperature (and a view from the top would reproduce the points of Fig. 1). Notice that the density ρ and the specific heat C_p vary by several orders of magnitude over the domain displayed, while the dynamic viscosity μ and the thermal conductivity λ vary by a factor of smaller than 4 only.

Finally, in order to assess possible contribution of compressibility to the NOB effects, we evaluate the Mach number $M = U_f/c = \sqrt{g\alpha\Delta T H}/c$, with isobaric thermal expansivity α and the speed of sound c obtained from HEPAK (not shown). The results show that for all experiments considered, the Mach numbers are in the range $M \lesssim 10^{-2}$ and guarantee that possible breaking of OB conditions due to compressibility can be neglected. Thus the NOB effects in RBC experiments with cryogenic helium stem solely from temperature dependencies of the fluid properties.

IV. EXPERIMENTS IN CRYOGENIC

^{4}He Cryogenic helium ^{4}He has been used to reach extreme turbulence intensity in "tabletop" RBC experiments on one hand thanks to the peculiar material properties near the CP allow to reach high Rayleigh numbers Ra, on the other hand, due to technical advantages, as heat leaks and many other parasitic effects are naturally highly suppressed in cryogenic conditions. The first advantage goes side by side with caveats of inevitably varying the Prandtl number $\mathrm{Pr} = \nu/\kappa$ [8,11] as well as NOB effects stemming from (21) and the dependencies (12)–(16). Here we reanalyze RBC data obtained at the Brno cryogenic turbulence facility [17].

The Brno experiment comprises a cryostat with a helium cryogenic experimental cell with the height $H = 0.3$ m and diameter $d = 0.3$ m (aspect ratio $\Gamma = d/H = 1$) with particular effort to minimize the influence of the cell structure and materials on the observed convection. The cell has been designed to withstand pressures of 3.5 bars to cover a range of Rayleigh numbers $10^7 \leqslant \mathrm{Ra} \leqslant 10^{15}$. Here we list the main features of the experimental cell only, including all crucial recent upgrades. In an ideal RBC experiment, the top and bottom plates should maintain nonfluctuating constant temperatures T_{top} and T_{bot} and the cell sidewalls should be adiabatic. The top and bottom plates of our cell are made of 28-mm-thick annealed OFHC copper of very high thermal conductivity of at least $\lambda_{\mathrm{Cu}} = 2$ kW m^{-1} K^{-1} at 5 K. Parasitic heat fluxes from the sidewalls into the working fluid are minimized by using very thin stainless steel sidewalls with thickness $\delta = 0.5$ mm and a thermal conductivity λ_w. A special design of the cell corners is used, see Fig. 4 in Ref. [17]. One way to estimate the influence of the sidewall on the heat transport is via the wall parameter $W = 4\delta\lambda_w/(\lambda_{\mathrm{He}}D)$; for our cell $0.22 > W > 0.15$ depending on actual value of the thermal conductivity for each data point. By correction, we mean a subtraction of the heat conducted by sidewalls from the heat that passes through the working fluid by convection [26]. We also paid attention to employ good thermal shielding and minimize other external parasitic heat flows into the cell which could substantially influence the convection dynamics.

A temperature correction which needs to be addressed in cryogenic experiments is that due to adiabatic gradient, g/C_p. It is given by $\Delta T_{\mathrm{ad}} = g\alpha H T_m/C_p = \tilde{D}T_m$, see also Eq. (21), which has to be subtracted from the measured temperature difference ΔT before evaluating Ra and comparing to the results of DNS based on Eqs. (4)–(6), otherwise the experimental data points would be very much off the expected Nu(Ra) dependencies. In typical large RBC cryogenic helium experiments, including the experiments in Brno, ΔT_{ad} is of order 1 mK. In the largest RBC cell at Oregon, it was about 3 mK [8]. In contrast, in turbulent RBC in air at room temperature the adiabatic gradient correction is not important, as $g/C_p = 0.01$ K/m; thus the scale height across which T drops by an order of magnitude is 1 km.

Cryogenic helium does not absorb thermal radiation, which leaves the radiation corrections to the Nusselt number negligibly small. We point to a straightforward evaluation in Ref. [27] and to the discussion of an extreme case in Ref. [28].

The top and bottom plates of the cell are equipped with four germanium (Ge) thermometers, calibrated at Physikalisch-Technische Bundesanstalt Berlin (Germany) up to the best currently available precision of ± 2 mK absolute accuracy over the entire temperature range of interest. These Ge thermometers are embedded in the middle and on the sides of both plates. We see no horizontal temperature gradients within Ge sensors accuracy of 2 mK in both copper plates. Following the last upgrade, both copper plates contain a pair of fast response Lakeshore DT-670 silicon (Si) diode thermometers, allowing to resolve the plate temperature fluctuations, which on one hand enable much better control of the temperature boundary conditions [16] compared to previous experiments via proportional-integrative-derivative feedback loops and, on the other hand, can be used to correlate dynamics of the turbulent large-scale circulation in the bulk with temperature fluctuations affecting the boundary layers. An additional set of germanium sensors of type TTR-G [29,30] is placed inside the bulk of the cell, as shown in Refs. [16,31]. Compared to the sensors in the plates, these sensors have the shape of very small 250-μm-sidelength Ge cubes. They have a minimal hydrodynamic impact on the flow and allow for a fast response. The sensors are calibrated *in situ* by us against the primary four sensors in the plates. To evaluate ξ_{NOB}, the central temperature T_c is determined from the time average of the resistance signals from TTR-G sensors located symmetrically with respect to both the horizontal midplane and the vertical axis of the cell. The resistance signals are recorded using the Lakeshore LS-350 temperature controller, with its calibration curves refined in situ. The experiments start after the flow reaches a statistically steady state and the duration of individual runs ranges typically between 30 min and 6 h. The signals are sampled at a frequency of 1 to 5 Hz.

V. NONLINEAR REGRESSION OF NON-BOUSSINESQ PARAMETERS

A. Experimental data base and regression procedure

We are interested in the dependence of the NOB parameter on state variables and material properties, i.e., most generally this results to a function $\xi(p_m, T_m, \Delta T, \alpha(T,p), \lambda(T,p), \mu(T,p), C_p(T,p), \rho(T,p))$. The perturbative expansion of Sec. II has reduced this high-dimensional function to one of thirteen input parameters. These are the mean pressure p_m, the mean temperature T_m, the temperature difference between bottom and top boundaries ΔT, and the expansion parameters ε_i for $i = 1, \ldots, 10$. The latter ones determine the first and second temperature derivatives of the material properties and state variables as summarized in Table I. The nonlinear regression proceeds in three levels of increasing complexity. We aim at reconstructing the following functions:

$$\xi_1 := \xi_{\mathrm{NOB}}(p_m, T_m, \Delta T), \tag{23}$$

$$\xi_2 := \xi_{\mathrm{NOB}}(p_m, T_m, \Delta T, \varepsilon_{2k+1}) \quad \text{for} \quad k = 0, \ldots, 4, \tag{24}$$

$$\xi_3 := \xi_{\mathrm{NOB}}(p_m, T_m, \Delta T, \varepsilon_k) \quad \text{for} \quad k = 1, \ldots, 10. \tag{25}$$

In the first approach ξ_1, no expansion parameter ε_i is used for the training of the neural network. It is explored how the NOB parameter depends on mean pressure and temperature as well as imposed temperature difference only. The result can serve as a baseline to forecast NOB effects on the temperature profile asymmetry $\xi_{\mathrm{NOB}}(p_m, T_m, \Delta T)$ in future experiments. In the more detailed successive steps, we are interested in a finer resolution of the effects of individual fluid properties on the temperature asymmetry. In the second (third) approach ξ_2 (ξ_3), sets of all linear-order (linear and quadratic-order) expansion coefficients ε_{2k+1} (ε_{2k}) are taken together as input data for a slightly deeper neural network architecture since the feature extraction proceeds in a higher-dimensional feature space. In this case, before calculating the non-Boussinesq parameter, it was necessary to perform preliminary calculations to determine ε_k at each point of the p-T space within the given ΔT by means of HEPAK. Values of the NOB parameters (23)–(25) are given in units of K throughout the paper.

TABLE II. Details of the deep neural network which is used for the first approach. The output shape consists of the batch size and the number of weights.

Layer	Output shape	Number of parameters
Linear	[16, 400]	1600
ReLU	[16, 400]	1
BatchNorm-1d	[16, 400]	800
Linear	[16, 1]	401
BatchNorm-1d	[16, 1]	2
Sigmoid	[16, 1]	0
Total		2804

B. First reconstruction method without expansion parameters

In the first reconstruction method, there are three input parameters, the mean pressure p_m and the mean temperature T_m which define the operating point of a particular laboratory measurements. The third input parameter is the applied temperature difference between the bottom and top plates. The only output parameter is the difference between mean temperature T_m and temperature T_c in the center of the layer, ξ_1, as already defined in the last subsection, see Eq. (23). For details on the network architecture, see Table II.

Figure 3 shows the reconstruction of $\xi_1(T, P)$ for four different outer temperature differences ΔT which are indicated in the title of Figs. 3(a), 3(b) 3(d), and 3(e). In Figs. 3(c) and 3(f), we display in addition the root-mean-square error (RMSE) contour plots for two cases which arises when taking

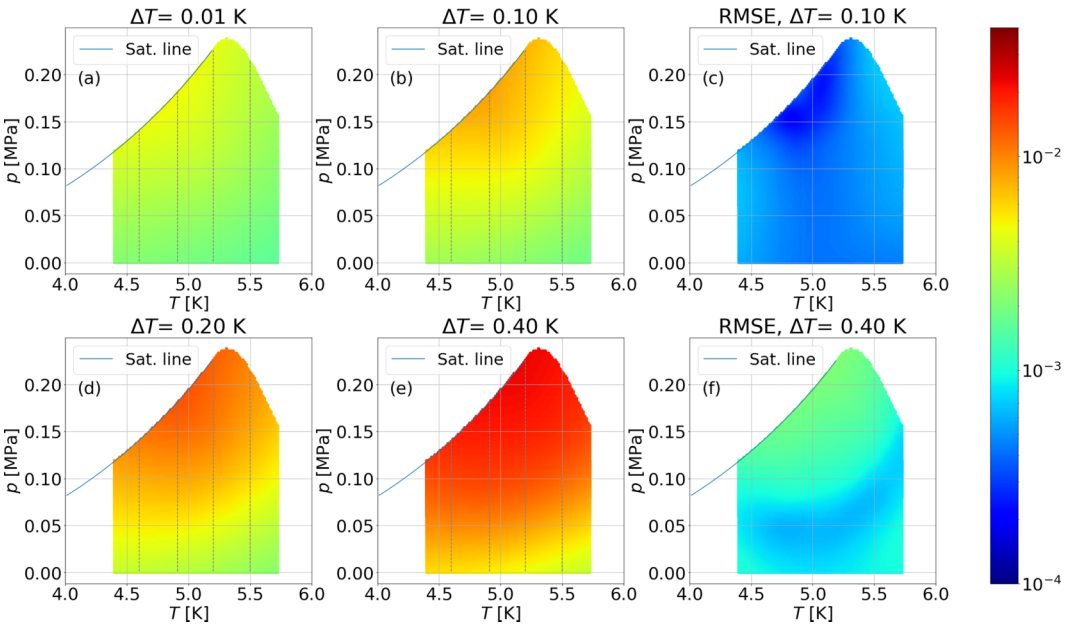

FIG. 3. Contour plots of the reconstruction of the non-Boussinesq parameter $\xi_1(p, T)$ for different ΔT is shown in panels (a), (b), (d), and (e). Panels (c) and (f) display the corresponding root-mean-square error (RMSE) for two of the four cases. The RMSE is given by Eq. (26). Unit for the color code is Kelvin.

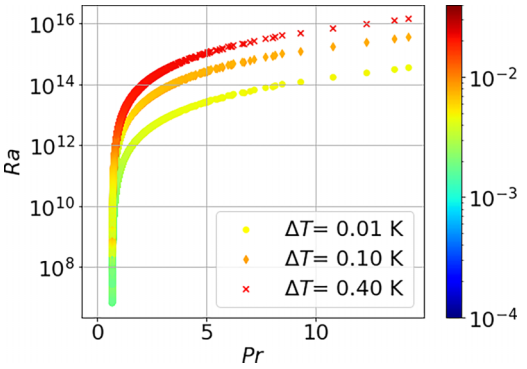

FIG. 4. Plot of ξ_1 in the Ra-Pr parameter space for three different outer temperature differences ΔT. The data points are color-coded by ξ_1 as given by the legend to the right. Unit for the color code is Kelvin.

the $i = 1, \ldots, N_{\text{rec}} = 100$ individual reconstructions. It is defined as

$$\text{RMSE}(p, T) = \sqrt{\frac{1}{N_{\text{rec}}} \sum_{i=1}^{N_{\text{rec}}} |\xi_k(i, T, p) - \overline{\xi}_k(T, p)|^2} \quad \text{for} \quad k = 1, 2, 3, \tag{26}$$

where $\overline{\xi}_k(T, p)$ the mean reconstructed surface. In Refs. 3(a), 3(b), 3(d), and 3(e), it can be seen that the maximum value of the NOB parameter is always reached in the vicinity of the phase boundary and at the critical point. As the temperature difference ΔT increases, the NOB parameter also increases. In Figs. 3(c) and 3(f), it is seen that the RMSE also increases for bigger ΔT. One reason is that there are less corresponding experimental data. The largest errors occur near the critical point at the end of the phase boundary.

The non-Oberbeck-Boussinesq parameter ξ_1 is also shown in Ra-Pr parameter space in Fig. 4 for three outer temperature differences ΔT, cf. Fig. 1(a) for an analogous display of experimental values. All branches for each ΔT start at $\text{Pr} = 0.7$ for the smallest Rayleigh numbers. When the Rayleigh number increases by eight orders of magnitude, the Prandtl number increases monotonically up to $\text{Pr} \simeq 15$. The data points are color coded by ξ_1. The NOB parameter also grows along the curves up to its highest values at $\text{Pr} \simeq 2$. With a further increase of the Prandtl number, the NOB parameter ξ_1 remains however nearly unchanged.

C. Second reconstruction method including linear-order ε parameters

For the next level, we reconstruct the parameter field ξ_2 with the linear order expansion parameters ε_i. Input parameters for the deep neural network are now mean pressure p_m, mean temperature T_m, outer temperature difference ΔT (as in the last case) together with all ε_{2k+1} for $k = 0, \ldots, 4$. The output is now the NOB parameter ξ_2 of Eq. (23). The neural network is detailed in Table III.

The results are shown in Fig. 5, in analogy with Fig. 3, for four different temperature differences. Also, we add again two root-mean-square error plots in Figs. 5(c) and 5(f) for $\Delta T = 0.1$ and 0.4, respectively. It can be seen that the qualitative behavior is similar to the results of the first reconstruction method. The difference between the reconstructions ξ_1 and ξ_2 is highlighted in Fig. 6, showing the deviation $|\xi_1 - \xi_2|$. Maximum deviations are up to $\xi \simeq 0.005$ K, observed for $\Delta T = 0.2$ K near the critical point and for $\Delta T = 0.4$ K in the lower-T part near the saturation curve (maximum relative value of $|\xi_1 - \xi_2|/\xi_1 \sim 40\%$). The graphs show that the influence of linear coefficients near the critical point grows as the temperature difference increases.

The Ra-Pr plots related to the $|\xi_1 - \xi_2|$ differences are shown in Fig. 7 and display the largest deviation near the critical point and at the saturation line when $\text{Pr} \gtrsim 2$ and Ra varying from 10^{12} to 10^{14}.

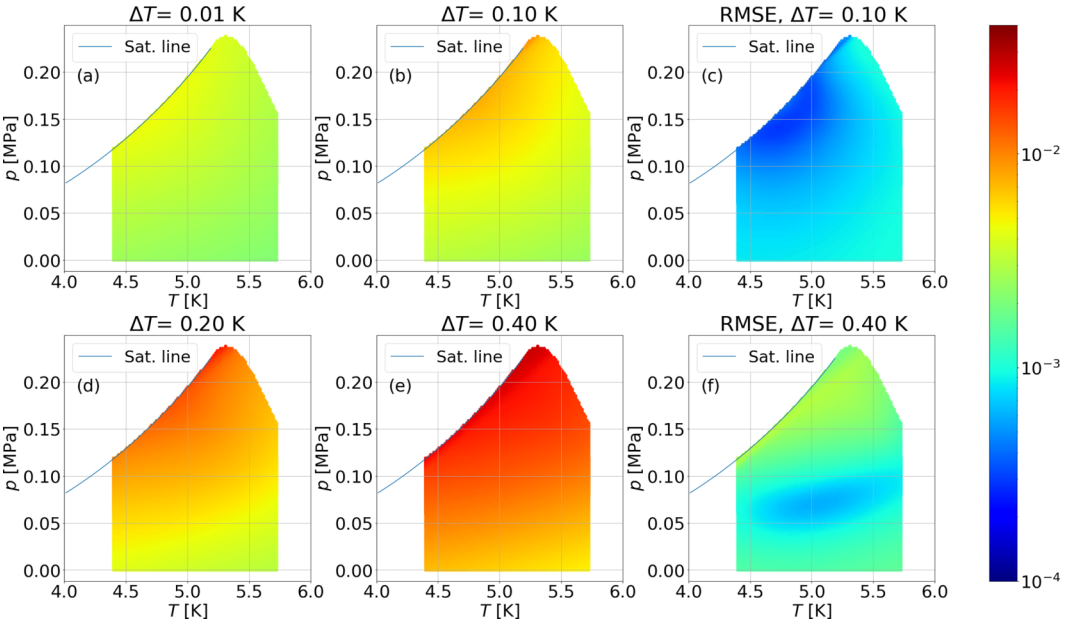

FIG. 5. Contour plots of the reconstruction of the non-Boussinesq parameter $\xi_2(p, T)$ for different ΔT is shown in (a), (b), (d), and (e). [(c) and (f)] The corresponding root-mean-square error (RMSE) for two of the four cases. The RMSE is given by Eq. (26). The unit for the color code is Kelvin.

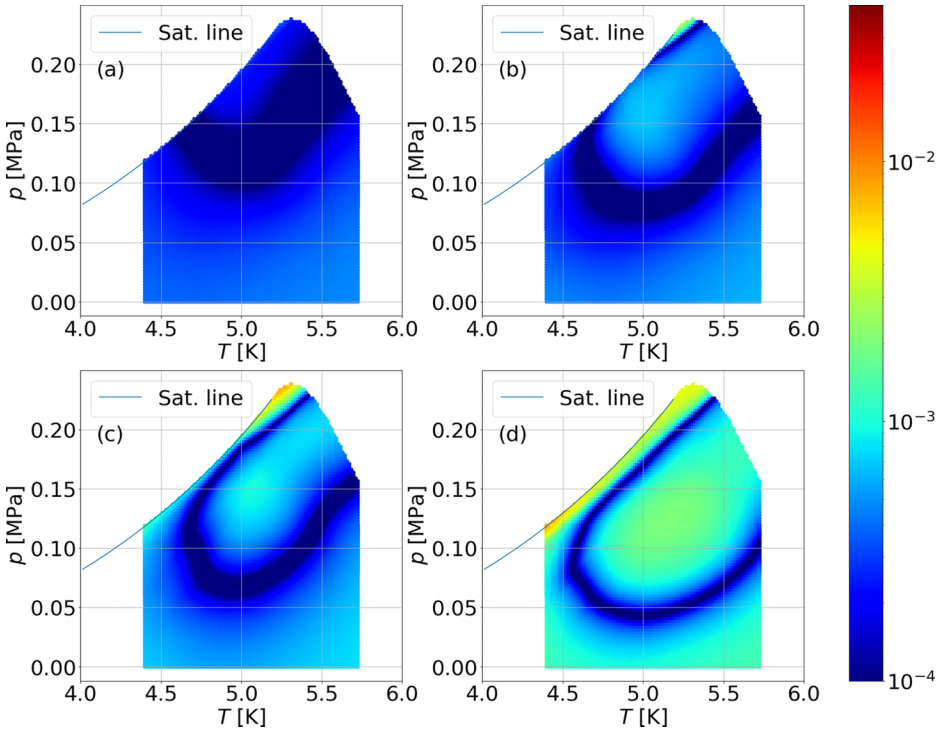

FIG. 6. Contour plots of the absolute difference $|\xi_1 - \xi_2|$ between the first and second reconstruction method in the p-T parameter plane for four different ΔT values which correspond to those in panels (a), (b), (d), and (e) of Figs. 3 and 5. The unit for the color code is Kelvin.

TABLE III. Details of the deep neural network which is used for the second approach. The output shape consists of the batch size and the number of weights for each network layer.

	Reconstruction of ξ_2		Evaluation of ε_{2i+1}	
Layer	Output shape	Number of parameters	Output shape	Number of parameters
Linear	[16, 400]	3600	[16, 500]	2000
PReLU	[16, 400]	1	[16, 500]	1
BatchNorm-1d	[16, 400]	800	[16, 500]	1000
Linear	[16, 1]	401	[16, 5]	2505
BatchNorm-1d	[16, 1]	2	[16, 5]	10
Sigmoid	[16, 1]	0	[16, 5]	0
Total		4804		5516

D. Third reconstruction method including quadratic-order ε parameters

The last reconstruction method includes 13 input parameters to obtain ξ_3. This comprises linear and quadratic expansions with respect to the temperature encoded by ε_i for $i = 1, \ldots, 10$. Our analysis shows that the absolute difference $|\xi_2 - \xi_3|$ remains very small for all the p_m, T_m, and ΔT values considered. This can be seen in Fig. 8, which corresponds to four "sections" through the $p - T$ plane at $T_m = 4.6$, 4.91, 5.2, and 5.5 K showing the p dependencies of ξ_1, ξ_2, and ξ_3. Finally, we refer to Appendix B, where we have summarized further error analysis for all three reconstruction methods. This analysis illustrates how strongly the 100 individual reconstructions of ξ_k vary when selecting different subsets as training and test data, see Fig. 10.

E. Discussion of the reconstruction methods

The results in Secs. V B–V D display a general trend for the magnitude of NOB effects in RBC in cryogenic helium gas quantified by the response parameters ξ_i, $i = 1, 2, 3$. All of them grow significantly as we increase pressure p_m and decrease temperature T_m towards the phase boundary at SVC and towards the CP. This is seen throughout Figs. 3 and 5 for different ΔT values, chosen here to cover the ranges of ΔT taken in high-Ra turbulent RBC experiments. Figure 8 shows in more detail the differences between individual reconstructions obtained by different neural network architectures. We can observe that while the differences between ξ_2 and ξ_3 are practically negligible, the reconstruction calculating ξ_1, involving only the basic experimental parameters, namely p_m, T_m,

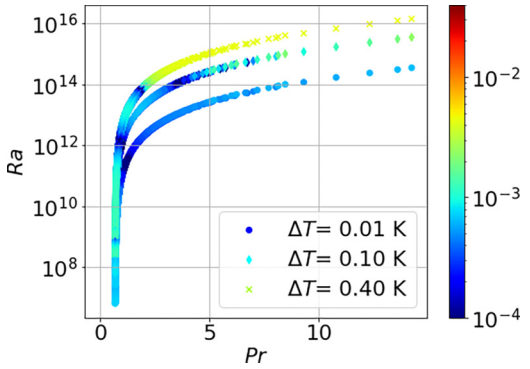

FIG. 7. The absolute difference $|\xi_1 - \xi_2|$ between the first and the second reconstruction method in the Ra-Pr parameter space for three different outer temperature differences ΔT (cf. Fig. 6). The unit for the color code is Kelvin.

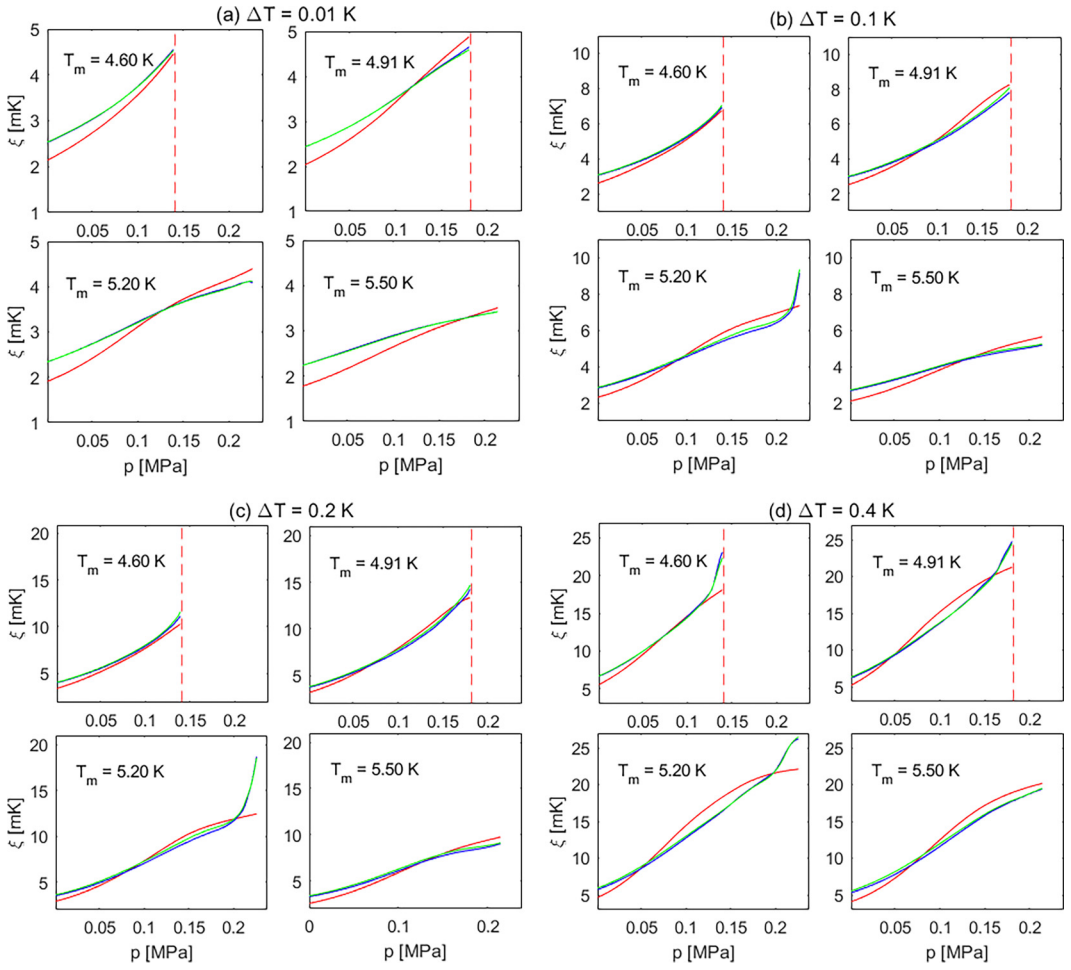

FIG. 8. Comparison of individual reconstructions of the NOB parameter ξ_1 (red), ξ_2 (blue), and ξ_3 (green) plotted as functions of pressure p at four values of $T_m = 4.6$, 4.91, 5.2, and 5.5 K (see insets in panels) and four values of $\Delta T = 0.01$, 0.1, 0.2, and 0.4 K (cf. Figs. 3 and 5). The vertical red dashed lines in panels with $T_m = 4.6$ K and 4.91 K denote the p values at the SVC.

and ΔT, significantly differ from ξ_2 and ξ_3, which in addition take into account the linear and quadratic terms in the expansion of the material properties of helium as a function of temperature, expressed by the dimensionless NOB control parameters ε_i, $i = 1, \ldots, 10$, given in Table I. In particular, ξ_2 and ξ_3 show much more pronounced growth at the phase boundary near the SVC and at the CP as a function of pressure than ξ_1. Further, the ξ_2 and ξ_3 curves are on average markedly more convex, while ξ_1 often grows in a more concave fashion towards the SVC and/or CP, see, e.g., the most pronounced case for $\Delta T = 0.2$ K and $T_m = 5.2$ K (very close to the critical temperature $T_{\mathrm{cri}} = 5.195$ K). Note that the occurrence of crossings of the concave regions of ξ_1 with convex parts of ξ_2 apparent in Fig. 8 explains appearance of tongue-shaped features (contours of $|\xi_1 - \xi_2| = 0$) seen in Fig. 6.

In addition to the three reconstructions (23)–(25) detailed in Secs. V B–V D, we performed also several four-parameter reconstructions taking individual ε_i, $i = 1, \ldots, 10$ one by one in addition to p_m, T_m, and ΔT within the appropriate neural network. Each of the results differed from the ξ_1

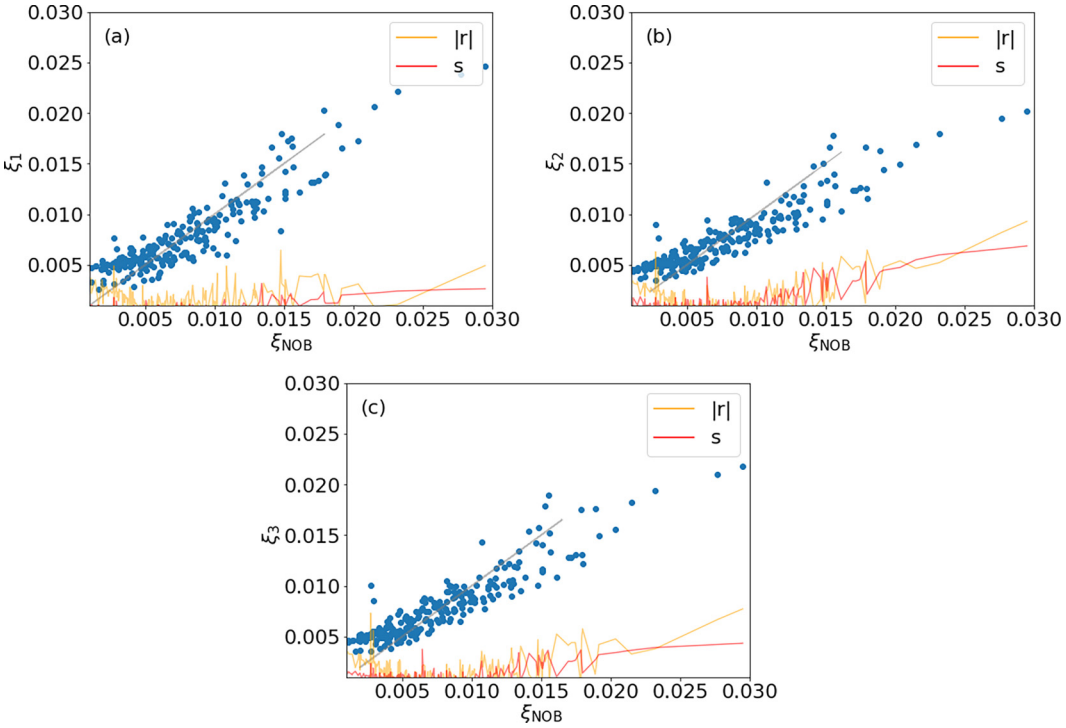

FIG. 9. Correlation of the reconstructed values of the NOB parameters ξ_1 (a), ξ_2 (b), and ξ_3 (c) of Eqs. (23)–(25) with the experimental values of ξ_{NOB} of Eq. (3). The gray line is the ideal fit for visual guidance. The red and yellow curves at the bottom of each panel represent the standard deviation s and the sum of residuals $|r|$ for the ensembles of $N_{\mathrm{rec}} = 100$ neural network runs to obtain each point, respectively; see Appendix B for details.

surfaces shown in Fig. 3 by less then the experimental accuracy of 3 mK. Thus only the combination of the linear expansion parameters, resulting in ξ_2 of Eq. (24), can be considered significant.

In Fig. 9, we finally plot the ξ_{NOB} results obtained by the machine learning (y axis) in comparison to the experimental data (x axis) for ξ_1 (a), ξ_2 (b), and ξ_3 (c). Each point thus corresponds to an experimental value and a value obtained from the neural network. In addition, a line $y = x$ for an ideal fit to the data is shown. The presented spread of points shows a fairly good reconstruction of the non-Boussinesq parameters by the ML algorithm.

VI. CONCLUSION AND OUTLOOK

In this work, we investigated the non-Oberbeck-Boussinesq behavior in high-Rayleigh-number laboratory experiments of turbulent Rayleigh-Bénard convection in cryogenic helium ^{4}He. The NOB effects in this experimental setup are shown to be caused by the temperature dependence of the material properties at the molecular level, while the compressibility effects can be neglected with a Mach number of $M \lesssim 10^{-2}$. The temperature T_c measured at the center of the RBC cell is found to deviate from the arithmetic mean of the temperatures of the copper plates at the top and bottom, T_m. This is an indicator of an asymmetry of the statistical properties between the top and bottom in the cell, which unambiguously signifies breaking of the OB approximation. The present study used this temperature deviation as the NOB indicator. These deviations have been determined in a series of experiments which provide a sparse data set to reconstruct the function $\xi_{\mathrm{NOB}}(p, T) = T_m - T_c$ by a nonlinear regression. The experiments are characterized by the operating

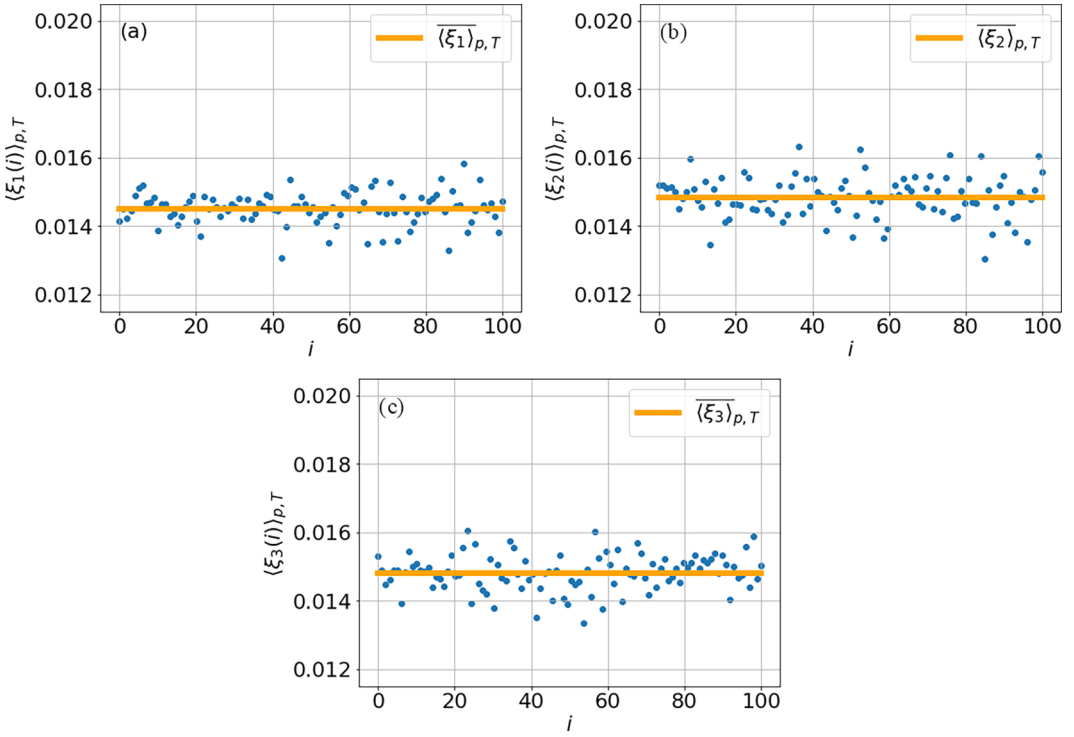

FIG. 10. Reconstructions of $\xi_i(T, p)$. Deviation from the mean of the 100 individual reconstructions. Points are $\langle\xi_i(i)\rangle_{p,T}$ and the solid line is $\overline{\langle\xi_i\rangle}_{p,T}$.

point in the pressure–temperature plane, (p_m, T_m), and the outer temperature difference, ΔT. We thus provide a smooth approximation (at different levels of accuracy) for the strength of the NOB effects with respect to two state variables.

In detail, we performed reconstructions of the NOB parameter by deep neural networks in three different ways. The first approach is based on the operating point p_m, T_m, and ΔT. The second and third approaches incorporate the expansion coefficients up to the linear and quadratic orders of the Taylor expansion with respect to $\delta T = T - T_m$ of the material properties and mass density, respectively. The comparison of the different methods can be summarized as follows: (i) The inclusion of the linear-order temperature expansion alters the reconstruction results by up to 40%. (ii) The inclusion of the second expansion order does not alter the magnitude of the NOB effects significantly. Our study provides a first systematic reconstruction of the NOB effects in experiments with cryogenic helium, and renders a set of maps for expected NOB effects in a wide area of the pressure-temperature plane for different values of ΔT in future experiments. A systematic analysis of the impact of the expansions on the heat and momentum transfer could be a next step which would require numerical investigations of the OB configuration for these parameters.

ACKNOWLEDGMENTS

The joint project is supported by Grant No. 21-06012J of the Czech Science Foundation (GAČR) for M.M. and by Grant No. SCHU 1410/31-1 of the Deutsche Forschungsgemeinschaft (DFG) for G.Z. The work of G.Z. is co-funded by the European Research Council (ERC, MesoComp, Grant No. 101052786). Views and opinions expressed are, however, those of the authors only and do not necessarily reflect those of the European Union or the European Research Council. Neither

the European Union nor the granting authority can be held responsible for them. Finally, we thank L. Skrbek, T. Králík, O. Shishkina, and V. Valori for discussions.

APPENDIX A: DETAILS OF THE DEEP NEURAL NETWORKS FOR NONLINEAR REGRESSION

In the following, we will provide some technical details of the machine learning methods that were used for the nonlinear regression analysis, see, e.g., Ref. [32]. In order to calculate all results, we had to use network models with different input and output parameters. They are provided in the following three tables together with some information. In the 1st model we trained a neural network without any information about the perturbative expansion as explained in the main text. The model consists of a total of six layers. These are (1) linear layers which apply a linear transformation of the incoming data followed by (2) a rectified linear unit (ReLU) function which performs an element-wise nonlinear activation. ReLU and the parametric ReLU (PReLU) are given by

$$\mathrm{ReLU}(x) = \max_x(0, x) \quad \text{and} \quad \mathrm{PReLU}(x) = \max(0, x) + a\min(0, x), \tag{A1}$$

for input data x with parameter $a > 0$. Furthermore, (3) the BatchNorm1d function of the PyTorch library is applied as a batch normalization to fix expectation value E and variance Var of the input in order to accelerate the training. This function is given by

$$\mathrm{BatchNorm1d}(x) = \frac{x - E[x]}{\sqrt{\mathrm{Var}[x] + \epsilon}}, \tag{A2}$$

for input data x in the form of a minibatch. Finally, (4) the sigmoid applies another element-wise nonlinear activation which is given by

$$\sigma(x) = \frac{1}{1 + \exp(-x)}. \tag{A3}$$

This first neural network in Table II obtains ξ_1 as the output resulting from three quantities at input, see Eq. (23). For our nonlinear regression task, there are, however, only 236 data points available to train the neural network. This is a small number for a full training of a deep neural network in the considered pressure-temperature interval. It can lead to the fact that in the randomly chosen input data for the training-testing procedure, no data point near the saturation line and the critical point is chosen at all. This in turn can result in an incorrect approximation of the non-Boussinesq parameter ξ_{NOB}. In order to remove this effect of an insufficient amount of experimental data, training and testing were performed in a cycle of 100 runs at each of the three levels. Each run takes a randomly chosen subsample of the RBC data and uses the rest for testing. The deviation of each calculation from the mean is shown in Appendix B. In this way, we obtained more robust regression results for a relatively small number of RBC experiments.

The second reconstruction method includes the parameters ε of the linear order expansion. These parameters, however, cannot be obtained close to the phase boundary from HEPAK and were thus reconstructed first by a neural network. The corresponding architecture is specified in the right fraction of Table III. Input is again p_m, T_m, and ΔT. With these input parameters, we obtain five outputs, namely ε_1, ε_3, ε_5, ε_7, and ε_9. Subsequently, we add them as further input parameters, i.e., we have a total of eight inputs to calculate the contour plot of ξ_2 in the p-T plane. The recursion is now more complicated in comparison to the first approach because all property gradients in the experimental data fluctuate strongly, particularly close to the phase boundary. Also, the model is more complex since it includes more parameters. The architecture of the neural network is basically the same for both substeps. The third reconstruction method is similar to the second. Now, we use linear and quadratic orders, reconstruct the 10 expansion coefficients first, and obtain ξ_3 from a network with 13 inputs. The architecture is specified in Table IV. It is basically similar to the second reconstruction approach.

TABLE IV. Details of the deep neural network which is used for the third approach. The output shape consists of the batch size and the number of weights.

	Reconstruction of ξ_3		Evaluation of ε_i	
Layer	Output shape	Number of parameters	Output shape	Number of parameters
Linear	[16, 400]	5600	[16, 500]	2000
PReLU	[16, 400]	1	[16, 500]	1
BatchNorm-1d	[16, 400]	800	[16, 500]	1000
Linear	[16, 1]	401	[16, 10]	5010
BatchNorm-1d	[16, 1]	2	[16, 10]	20
Sigmoid	[16, 1]	0	[16, 10]	0
Total		6804		8031

APPENDIX B: ERROR ANALYSIS OF THE NONLINEAR REGRESSION

Figure 10 shows the deviations of the $N_{\mathrm{rec}} = 100$ individual reconstructions, which are indexed with i, of the non-Boussinesq parameter $\langle \xi_k(i) \rangle_{p,T}$ from the mean of all calculations for $k = 1$, 2, and 3. We therefore first average the reconstructed field $\xi_k(T, P)$ over the p-T plane which is indicated by $\langle \cdot \rangle_{p,T}$. The mean non-Boussinesq parameter is eventually obtained by

$$\overline{\langle \xi_k \rangle}_{p,T} = \frac{1}{N_{\mathrm{rec}}} \sum_{i=1}^{N_{\mathrm{rec}}} \langle \xi_k(i) \rangle_{p,T} \quad \text{for} \quad k = 1, 2, 3. \tag{B1}$$

[1] L. P. Kadanoff, Turbulent heat flow: Structures and scaling, Phys. Today **54**, (8) 34 (2001).

[2] G. Ahlers, S. Grossmann, and D. Lohse, Heat transfer and large scale dynamics in turbulent Rayleigh-Bénard convection, Rev. Mod. Phys. **81**, 503 (2009).

[3] F. Chillà and J. Schumacher, New perspectives in turbulent Rayleigh-Bénard convection, Eur. Phys. J. E **35**, 58 (2012).

[4] M. K. Verma, *Physics of Buoyant Flows* (World Scientific, Singapore, 2018).

[5] X. He, D. Funfschilling, H. Nobach, E. Bodenschatz, and G. Ahlers, Transition to the Ultimate State of Turbulent Rayleigh-Bénard Convection, Phys. Rev. Lett. **108**, 024502 (2012).

[6] X. He, D. Funfschilling, E. Bodenschatz, and G. Ahlers, Heat transport by turbulent Rayleigh-Bénard convection for $\mathrm{Pr} \simeq 0.8$ and $4 \times 10^{11} \lesssim Ra \lesssim 2 \times 10^{14}$: Ultimate-state transition for aspect ratio $\Gamma = 1.00$, New J. Phys. **14**, 063030 (2010).

[7] X. Chavanne, F. Chillà, B. Castaing, B. Hébral, B. Chabaud, and J. Chaussy, Observation of the Ultimate Regime in Rayleigh-Bénard Convection, Phys. Rev. Lett. **79**, 3648 (1997).

[8] J. J. Niemela, L. Skrbek, K. R. Sreenivasan, and R. J. Donelly, Turbulent convection at very high Rayleigh numbers, Nature (Lond.) **404**, 837 (2000).

[9] J. J. Niemela and K. R. Sreenivasan, Confined turbulent convection, J. Fluid Mech. **481**, 355 (2003).

[10] P.-E. Roche, F. Gauthier, R. Kaiser, and J. Salort, On the triggering of the ultimate regime of convection, New J. Phys. **12**, 085014 (2010).

[11] P. Urban, V. Musilová, and L. Skrbek, Efficiency of Heat Transfer in Turbulent Rayleigh-Bénard Convection, Phys. Rev. Lett. **107**, 014302 (2011).

[12] P. Urban, P. Hanzelka, T. Králík, V. Musilová, A. Srnka, and L. Skrbek, Effect of Boundary Layers Asymmetry on Heat Transfer Efficiency in Turbulent Rayleigh-Bénard Convection at Very High Rayleigh Numbers, Phys. Rev. Lett. **109**, 154301 (2012).

[13] P. Urban, P. Hanzelka, T. Králík, M. Macek, V. Musilová, and L. Skrbek, Elusive transition to the ultimate regime of turbulent Rayleigh-Bénard convection, Phys. Rev. E **99**, 011101(R) (2019).
[14] P.-E. Roche, The ultimate state of convection: A unifying picture of very high Rayleigh numbers experiments, New J. Phys. **22**, 073056 (2020).
[15] P. Urban, P. Hanzelka, V. Musilová, T. Králík, M. La Mantia, A. Srnka and L. Skrbek, Heat transfer in cryogenic helium gas by turbulent Rayleigh–Bénard convection in a cylindrical cell of aspect ratio 1, New J. Phys. **16**, 053042 (2014).
[16] P. Urban, T. Králík, M. Macek, P. Hanzelka, T. Věžník, and L. Skrbek, Effect of boundary conditions in turbulent thermal convection, Europhys. Lett. **134**, 34003 (2021).
[17] P. Urban, P. Hanzelka, T. Králík, V. Musilová, L. Skrbek, and A. Srnka, Helium cryostat for experimental study of natural turbulent convection, Rev. Sci. Instrum. **81**, 085103 (2010).
[18] V. D. Arp, R. D. McCarty, and D. G. Friend, *Thermophysical Properties of Helium-4 from 0.8 to 1500K with Pressures to 2000MPa*, National Institute of Standards and Technology, Technical Note 1334 (NIST, 1998).
[19] http://htess.com.
[20] D. D. Gray and A. Giorgini, The validity of Boussinesq approximation for liquids and gases, Int. J. Heat Mass Transfer **19**, 545 (1976).
[21] O. Shishkina, S. Weiss, and E. Bodenschatz, Conductive heat flux in measurements of the Nusselt number in turbulent Rayleigh-Bénard convection, Phys. Rev. Fluids **1**, 062301(R) (2016).
[22] S. Weiss, X. He, G. Ahlers, E. Bodenschatz, and O. Shishkina, Bulk temperature and heat transport in turbulent Rayleigh-Bénard convection of fluids with temperature-dependent properties, J. Fluid Mech. **851**, 374 (2018).
[23] H. Yik, V. Valori, and S. Weiss, Turbulent Rayleigh-Bénard convection under strong non-Oberbeck-Boussinesq conditions, Phys. Rev. Fluids **5**, 103502 (2020).
[24] G. K. Batchelor, *The Theory of Homogeneous Turbulence* (Cambridge University Press, Cambridge, UK, 1960).
[25] J. Verhoeven, T. Wiesehöfer, and S. Stellmach, Anelastic versus fully compressible turbulent Rayleigh-Bénard convection, Astrophys. J. **805**, 62 (2015).
[26] P.-E. Roche, B. Castaing, B. Chabaud, B. Hébral, and J. Sommeria, Side wall effects in Rayleigh Bénard experiments, Eur. Phys. J. B **24**, 405 (2001).
[27] P. Urban, T. Králík, P. Hanzelka, V. Musilová, T. Věžník, D. Schmoranzer and L. Skrbek, Thermal radiation in Rayleigh-Bénard convection experiments, Phys. Rev. E **101**, 043106 (2020).
[28] S. Lepot, S. Aumaïtre, and B. Gallet, Radiative heating achieves the ultimate regime of thermal convection, Proc. Natl. Acad. Sci. USA **115**, 8937 (2018).
[29] V. F. Mitin *et al.*, Ge-on-GaAs film resistance thermometers for cryogenic applications, Cryogenics **47**, 474 (2007).
[30] V. F. Mitin, V. V. Kholevchuk, and B. P. Kolodych, Ge-on-GaAs film resistance thermometers: Low-temperature conduction and magnetoresistance, Cryogenics **51**, 68 (2011).
[31] V. Musilová, T. Králík, M. La Mantia, M. Macek, P. Urban and L. Skrbek, Reynolds number scaling in cryogenic turbulent Rayleigh-Bénard convection in a cylindrical aspect ratio one cell, J. Fluid Mech. **832**, 721 (2017).
[32] I. Goodfellow, Y. Bengio, and A. Courville, *Deep Learning* (MIT Press, Cambridge, MA, 2016).